Structure and hyperfine interactions of melt-spun $Fe_{80}Mo_7X_1B_{12}$ (X = Cu or Au) before and after transformation into nanocrystalline states

2002 J. Phys.: Condens. Matter 14 1249

(http://iopscience.iop.org/0953-8984/14/6/312)

INSTITUTE OF PHYSICS PUBLISHING JOURNAL OF PHYSICS: CONDENSED MATTER

J. Phys.: Condens. Matter **14** (2002) 1249–1260 PII: S0953-8984(02)30606-4

Structure and hyperfine interactions of melt-spun $Fe_{80}Mo_7X_1B_{12}$ (X = Cu or Au) before and after transformation into nanocrystalline states

M Miglierini[1], I Tóth[1], M Seberíni[1], E Illeková[2] and B Idzikowski[3]

[1] Department of Nuclear Physics and Technology, Slovak University of Technology, Ilkovičova 3, 812 19 Bratislava, Slovakia
[2] Institute of Physics, Slovak Academy of Sciences, Dúbravská cesta 9, 842 28 Bratislava, Slovakia
[3] Institute of Molecular Physics, Polish Academy of Sciences, M Smoluchowskiego 17, 60–179 Poznan, Poland

Received 8 November 2001, in final form 15 January 2002
Published 1 February 2002
Online at stacks.iop.org/JPhysCM/14/1249

Abstract

Mössbauer spectrometry (^{57}Fe transmission and conversion-electron techniques), differential scanning calorimetry, and x-ray diffraction are employed to study the microstructure and magnetism of amorphous and nanocrystalline $Fe_{80}Mo_7X_1B_{12}$ (X = Cu, Au) alloys. Heat treatment of amorphous specimens below the temperature of primary crystallization causes structural relaxation that, in turn, stabilizes the amorphous arrangement. Changes observed in the topological short-range order are more pronounced for X = Au because this alloy shows a higher degree of disorder in the bulk of the as-quenched state. For both alloys, three-step crystallization behaviour is observed.

Annealing performed in temperature range of the first crystallization provided different amounts of body-centred-cubic Fe nanograins. Magnetic interactions among them and their impact on the surrounding amorphous residual matrix are discussed using hyperfine-field distributions. Differences in hyperfine interactions between surface regions and bulk of the alloys are revealed from conversion-electron Mössbauer spectrometry and transmission Mössbauer effect measurements, respectively. The magnetic behaviours for X = Cu and Au are very similar after annealing at temperatures close to and beyond the end of the first crystallization peak. The impact of which element is present on the microstructure and magnetism is crucial during the commencement of the crystallization but it cannot be discerned for higher crystalline contents.

1. Introduction

Nanocrystalline Fe–M–B (M = Zr, Hf, or Nb) alloys prepared by controlled annealing of amorphous precursors are interesting because of their soft-magnetic properties (high saturation magnetization, high permeability, low core losses) [1], which can lead to possible magnetic applications [2]. Ultrafine grain structure featuring crystalline grains of the order of nanometres embedded in a residual amorphous matrix is responsible for this excellent magnetic behaviour [3]. The desired properties can be tailored by varying such parameters as composition, and preparation and annealing conditions, in order to build up crystalline grains in appropriate numbers and of appropriate dimensions [4]. Magnetic interactions among the nanograins consequently govern the resulting macroscopic attributes. In order to understand such a two-phase magnetic system, diverse methods of both structural and magnetic analysis are applied. Especially useful results are provided by microscopic techniques [5] that are able to track contributions from individual atoms. Among them, Mössbauer spectrometry plays a unique role, providing a chance to probe the structural arrangement and magnetic states of resonant atoms at the same time [6].

With the appearance of Si-free nanocrystalline alloys [7], new perspectives were opened up for Mössbauer spectrometry. The first crystallization step of these, the so-called NANOPERM alloys, is accompanied by formation of a bcc Fe phase that is actually a calibration material for Mössbauer effect measurements, and its hyperfine parameters are well known. For this reason, we have chosen the $Fe_{80}Mo_7X_1B_{12}$ (X = Cu, Au) system for detailed investigations. Another aspect, which we have considered, is the magnetic ordering temperature. Choosing this appropriately simplifies the Mössbauer spectra and offers a unique opportunity to study the onset of magnetic interactions inside an originally paramagnetic amorphous phase, which surrounds the ferromagnetic nanocrystals. One of the aims of this paper is to compare the effects of Cu and Au on the formation of nanocrystalline structure and their impact on the magnetic microstructure. Surface regions (down to a depth of about 100 nm) and the bulks of the alloys studied are compared from the point of view of structure and magnetic arrangement.

2. Experimental details

Amorphous ribbons (3.5 mm wide, about 25 μm thick) of $Fe_{80}Mo_7X_1B_{12}$ (X = Cu, Au) nominal composition were prepared by a single-roller technique on a Cu wheel in an Ar atmosphere. Nanocrystalline samples were prepared by 1 h thermal treatments of as-quenched precursors at different temperatures to produce varying amounts of bcc Fe nanocrystals. A protective Ar atmosphere was used to prevent oxidation.

Transmission ^{57}Fe Mössbauer spectrometry (TMS) was performed at room temperature with a ^{57}Co(Rh) source using a conventional constant-acceleration apparatus. Conversion-electron Mössbauer spectrometry (CEMS) was applied to the dull side of the ribbons using a home-made detector [8]. Fitting of the spectra (for details see e.g. [9]) was accomplished by combination of distributions of hyperfine fields $P(B)$. Crystalline phases were reconstructed from sextets of Lorentzian lines. We considered equal line intensity ratios for all spectral components as in [10]. Paramagnetic spectra were reconstructed from distributions of quadrupole splittings $P(\Delta)$. To account for the spectrum asymmetry, a linear correlation between the hyperfine magnetic field and/or quadrupole splitting and the isomer shift was introduced.

Structural characterization was performed by means of (along with Mössbauer techniques) x-ray diffraction using Co Kα radiation. The crystallization behaviour of the as-quenched

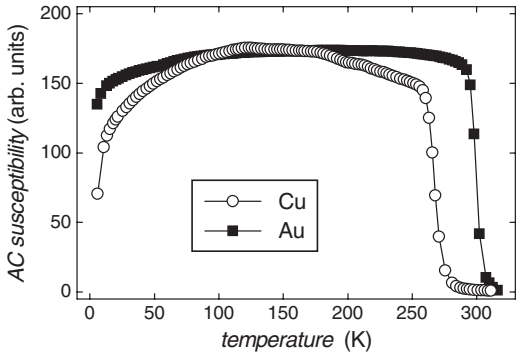

Figure 1. The temperature dependence of the in-phase ac susceptibility for $Fe_{80}Mo_7X_1B_{12}$ alloy; X = Cu: open circles; X = Au: solid squares.

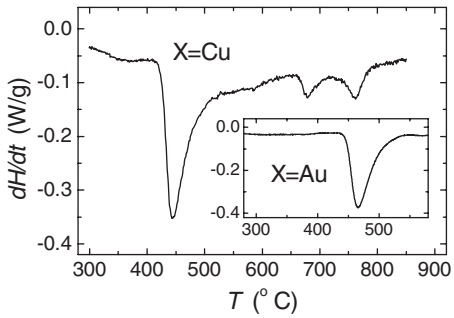

Figure 2. The DSC linear-heating curve (normalized heating power dH/dt versus temperature, T) of $Fe_{80}Mo_7X_1B_{12}$ as-quenched alloys; X = Cu—main figure; X = Au—inset.

samples was examined by means of both linear heating and isothermal differential scanning calorimetry (DSC) using Al sample pans and an Ar atmosphere. A linear-heating rate of 10 K min^{-1} was used. Isothermal measurements were performed after a 20 K min^{-1} linear-heating ramp.

The in-phase component of the ac susceptibility was measured as a function of temperature at the frequency of 130 Hz in an ac field of 1 Oe using a commercial Oxford susceptometer.

3. Results and discussion

3.1. Susceptibility measurements, DSC and XRD

The ac susceptibility versus temperature is displayed in figure 1. The transition from the ferromagnetic to the paramagnetic state takes place at around room temperature. The Curie temperatures for the X = Cu and X = Au samples were determined as 265 and 298 K, respectively.

The DSC linear-heating curve for X = Cu in figure 2 exhibits three exothermic peaks. The first crystallization peak for X = Au is enlarged as an inset in figure 2. The temperature of the onset of crystallization T_{x1} = 410 and 430 °C for Cu and Au samples, respectively. This temperature is associated with nucleation and growth of a new phase. Using XRD, the observed phase was identified as bcc Fe (see also figure 2 in [11]).

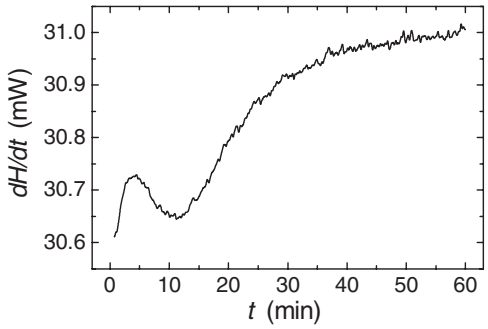

Figure 3. The isothermal DSC trace (heating power dH/dt versus time, t) for primary crystallization in $Fe_{80}Mo_7Au_1B_{12}$ alloy at 425 °C.

To investigate the kinetics of crystallization, we took an isothermal DSC trace slightly below T_{x1}. As seen from figure 3 where the results for X = Au ($T_{iso} = 425$ °C) are presented, the crystallization proceeds in a similar way to in classical FINEMET-type alloys [12]. A bell-shaped peak corresponds to a nucleation-and-growth-type transformation that can be described by the Johnson–Mehl–Avrami equation.

On the basis of the results from DSC experiments, for X = Cu we have chosen the annealing temperatures $T_a = 410$, 440, 470, 520, and 580 °C. For X = Au, heat treatments were performed at $T_a = 425$, 440, 470, 530, and 620 °C. Both ranges cover completely the first crystallization peaks, thus ensuring different amounts of bcc Fe crystalline grains in the nanocrystalline samples.

As confirmed by the XRD, the specimens were fully amorphous below T_{x1}. The DSC curves in figure 2, however, disclose some heat release by a distinct local minimum around 350 °C. This heat is liberated by structural relaxation of the as-quenched amorphous structure [13] which has excess free volume and experiences extraordinary stresses created during the preparation procedure. Release of stresses and the excess free volume lead to stabilization of the structure. Consequently, rearrangements of constituent atoms induce changes in the local short-range order (SRO). With the aim of tracking SRO deviations we have performed annealing in this temperature region also, selecting $T_a = 250$, 300, 350, and 380 °C for X = Cu and $T_a = 290$, 350, 380, and 410 °C for X = Au.

In the following sections we discuss Mössbauer spectrometry results obtained for specimens annealed below T_{x1} as well as in the temperature zone of the first crystallization.

3.2. Mössbauer spectrometry

3.2.1. Annealing below T_{x1}. Typical examples of room temperature ^{57}Fe transmission Mössbauer spectra of $Fe_{80}Mo_7Au_1B_{12}$ alloy are introduced in the left-hand panel of figure 4. Spectra corresponding to an as-quenched ribbon and a sample annealed for 1 h at $T_a = 380$ °C are presented. Because no traces of magnetically split components were found, the spectra were taken in a narrow velocity range to allow precise characterization. Both exhibit doublet-like structure that indicates paramagnetic behaviour and fully amorphous structure. The spectra were evaluated by using distributions of the quadrupole splitting $P(\Delta)$. A linear correlation between the quadrupole splitting and isomer shift was used to account for the observed line asymmetry. The resulting $P(\Delta)$ can be seen in the right-hand panel of figure 4.

A remarkable narrowing of $P(\Delta)$ corresponding to the 380 °C annealed sample with respect to that for the as-quenched one can be recognized. This can be interpreted in terms of a higher degree of 'order' in the amorphous structure. In other words, structural relaxation

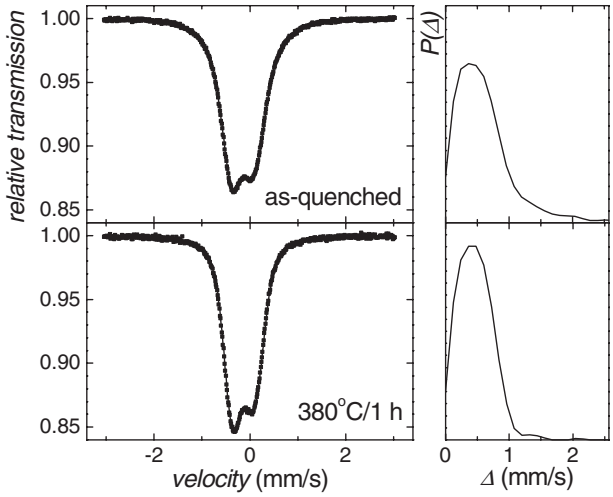

Figure 4. Room temperature transmission ^{57}Fe Mössbauer spectra (left-hand panel) and their corresponding distributions of quadrupole splitting, $P(\Delta)$ (right-hand panel), for as-quenched $Fe_{80}Mo_7Au_1B_{12}$ alloy and the sample annealed for 1 h at 380 °C.

caused by heat treatment releases stresses and reduces the excess free volume induced in the as-quenched alloy during the rapid quenching of the melt. Constituent atoms tend to occupy energetically more favourable positions inside disordered structure, which leads to changes in the chemical and/or topological SRO. The latter are subsequently demonstrated by a narrowing of the respective $P(\Delta)$ distributions. These changes can also be identified directly from the spectra. Narrowing of spectral lines increases the relative intensity of the lines. Simultaneously, more pronounced line asymmetry is observed. Similar, though less obvious, changes were identified also in the X = Cu alloy.

Mean values of the $P(\Delta)$ distributions, $\langle\Delta\rangle$, are illustrated in figure 5 together with their standard deviations, σ, as a function of annealing temperature T_a for X = Cu and Au (the connecting lines are only guides to the eye). The experimental errors of about ± 0.002–± 0.006 mm s^{-1} are smaller than the size of the symbols used. The standard deviation σ can serve as a quantitative measure of SRO and permits one to estimate the degree of structural (dis)order. High σ means that the structure is rather chaotic, whereas its decrease indicates a tendency toward closer packing.

Comparing σ-values for the as-quenched Cu- and Au-containing alloys in figure 5(*b*), we can conclude that a higher degree of disorder is observed in the bulk of X = Au than in X = Cu alloys. This might be associated with the approximately 14% bigger size of Au atoms which is also thought to be responsible for a striking difference in the distribution of electric field gradients suggested by the notably higher $\langle\Delta\rangle$ value for the X = Au as-quenched alloy in figure 5(*a*). Rather steep decreases in the values of $\langle\Delta\rangle$ and σ up to $T_a = 380$ °C suggest effective relaxation process, as identified also from the DSC curves in figure 2. Sudden increase in both parameters witnesses the presence of surface crystallization.

The evolutions of the curves for $\langle\Delta\rangle$ and σ with T_a for X = Cu do not show appreciable deviations up to 350 °C. An increase in $\langle\Delta\rangle$ and σ for the 380 °C annealed sample is ascribed to the onset of surface crystallization. It should be noted that the crystallites are formed only in surface layers and that is why they cannot be identified as distinct magnetic spectral components by TMS, which is a bulk technique. An indirect proof is, however, provided by a

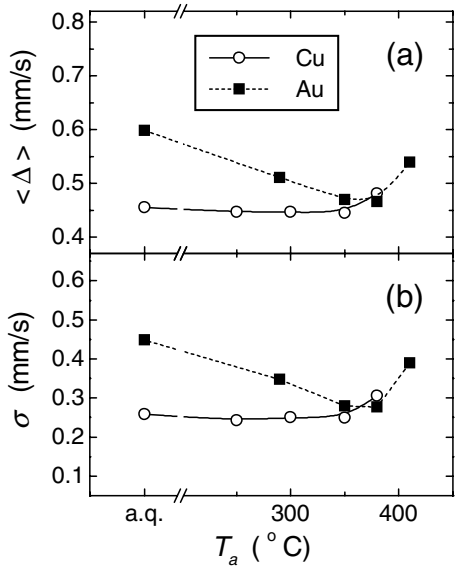

Figure 5. Average values, $\langle\Delta\rangle$, of quadrupole splitting distributions $P(\Delta)$ (*a*) and their standard deviation, σ (*b*), plotted against annealing temperature, T_a, for $Fe_{80}Mo_7X_1B_{12}$ alloy derived from TMS; X = Cu: open circles; X = Au: solid squares. Connecting lines are only guides to the eye.

sudden increase in the values of $\langle\Delta\rangle$ and (mainly) σ. Such a small amount of crystalline phase is far beyond the detection limit of the XRD technique.

To prove the presence of surface crystallization we have employed CEMS. This technique scans the surface layers down to a maximum depth of about 100 nm. Figure 6 introduces CEM spectra taken at room temperature for X = Cu samples annealed at 350 and 380 °C. The existence of bcc Fe (about 11%) is clearly demonstrated in the latter. The corresponding $P(\Delta)$ distribution is accompanied by a $P(B)$ distribution (relative amount 9%, average field 29.0(3) T) which is assigned to Fe atoms localized on the surface of bcc nanograins as well as in their immediate vicinity [9].

Quantitative features of $P(\Delta)$, comprising values of $\langle\Delta\rangle$ and σ, are presented in figure 7 for both compositions. Distinctions between X = Cu and Au alloys are not so pronounced as for the bulk (figure 5). In conclusion, the SRO of the surface regions of the alloys annealed below the temperature of the onset of crystallization is similar regardless of the choice of X. Surface crystallization starts, however, earlier than at T_{x1} by approximately 25 °C. The decrease of the crystallization temperature at the surface was attributed to the boron depletion of the surface regions in $Fe_{81}Zr_7B_{12}$ alloys [14], and similar effects were observed for $Fe_{80}Ti_7B_{12}Cu_1$ alloy [15]. Consequently, different SRO is observed in the bulk and on the surface of the alloys investigated, as will be discussed in more depth at the end of the following section.

3.2.2. Annealing in the temperature range of primary crystallization. Representative transmission ^{57}Fe Mössbauer spectra of $Fe_{80}Mo_7X_1B_{12}$ alloy annealed at the temperatures indicated are presented in figures 8(*a*) and (*b*) for X = Cu and Au, respectively. Corresponding hyperfine-field distributions $P(B)$ are plotted alongside the spectra. Mössbauer spectra consist of sharp lines superimposed upon broadened components. The former correspond to crystalline bcc Fe phase (CR). The latter are assigned to residual amorphous phase (AM) as well as to Fe atoms located on the surface of nanocrystalline bcc Fe grains that are in close contact with the

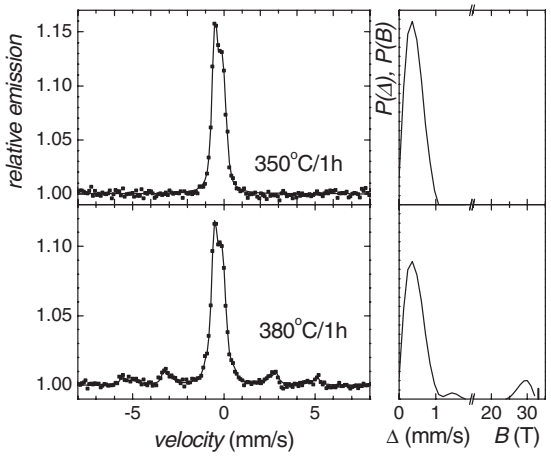

Figure 6. Room temperature CEMS (left-hand panel) and the corresponding distributions of quadrupole splitting, $P(\Delta)$ (right-hand panel), for the $Fe_{80}Mo_7Cu_1B_{12}$ alloy annealed for 1 h at 350 and 380 °C.

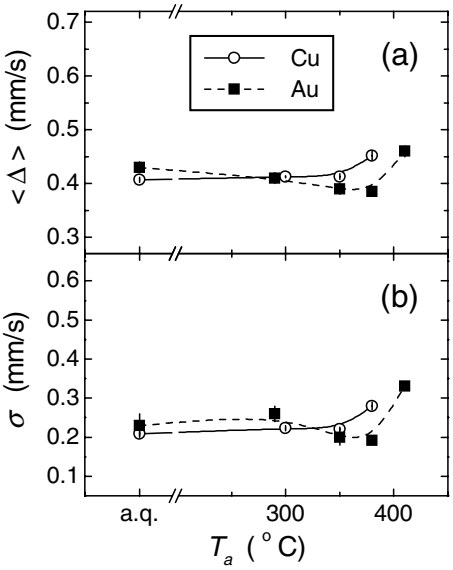

Figure 7. Average values, $\langle\Delta\rangle$, of the quadrupole splitting distributions $P(\Delta)$ (*a*) and their standard deviation, σ (*b*), plotted against annealing temperature, T_a, for $Fe_{80}Mo_7X_1B_{12}$ alloy derived from CEMS; X = Cu: open circles; X = Au: solid squares (connecting lines are only guides to the eye).

amorphous surrounding, the so-called interface zone (IF) [9]. Individual subspectra are shown in figure 8, too.

A substantial difference in shape of the spectra for the alloys annealed below T_{x1} presented in figure 4 and above the onset of crystallization is immediately obvious. The latter spectra displayed in figure 8 no longer exhibit pure quadrupole doublets. Instead, rather complicated patterns are observed. Specimens annealed at the crystallization onset temperature (X = Au, $T_a = 425$ °C) or slightly beyond this temperature (X = Cu, $T_a = 410$ °C) contain about 7 and

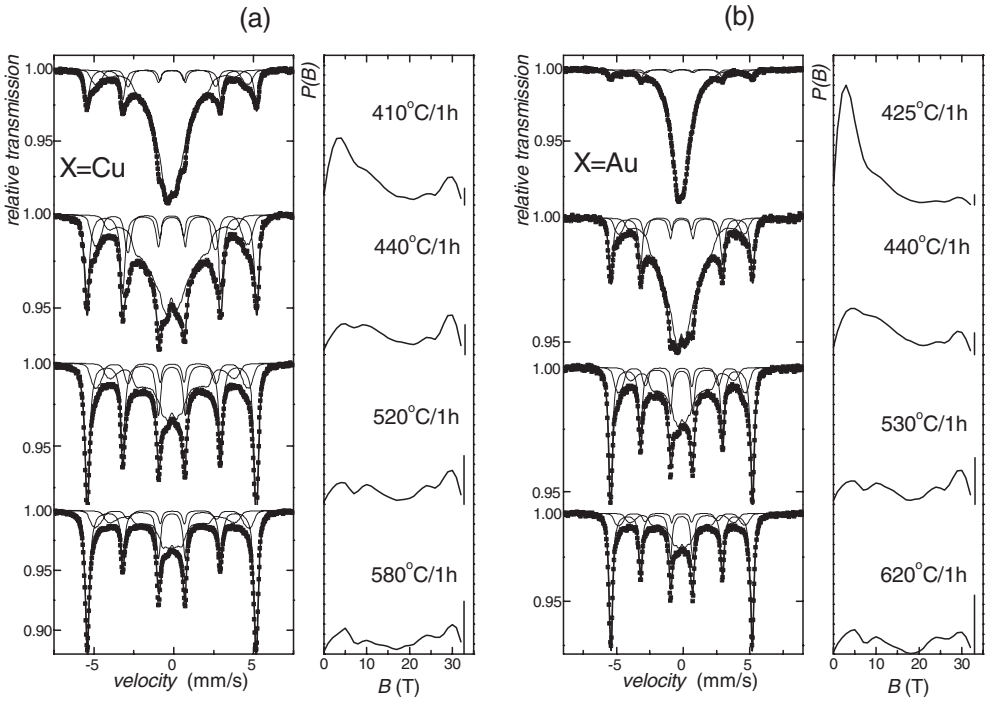

Figure 8. Room temperature transmission ^{57}Fe Mössbauer spectra (left side of panel) and corresponding distributions of hyperfine fields, $P(B)$ (right), for $Fe_{80}Mo_7X_1B_{12}$ alloy, with X = Cu (*a*), X = Au (*b*) annealed at the temperatures indicated for 1 h.

17% of bcc Fe phase, which is demonstrated by the magnetically split sextuplets of spectral lines positioned around the considerably broadened central AM component. This excess broadening is due to the occurrence of magnetic regions within the AM that were induced by exchange interactions among ferromagnetic bcc Fe nanocrystals [10, 16–18]. As the contribution of the CR and/or IF rises on account of the presence of the AM with increasing T_a, the Mössbauer spectra exhibit well-resolved six-line features. The $P(B)$ distributions reflect these changes in magnetic structure in a decrease of the low-B peaks and rising importance of the high-B values.

Results from the CEMS measurements are depicted in figure 9. The spectra exhibit similar features to those obtained by TMS. Two types of distinction can be noted, however. The line intensities of the sextet components indicate that the magnetic moments are positioned preferentially in the plane of a ribbon-shaped sample. This is true only for surface regions, as a consequence of the closed domain structure [19]. The substantial decrease in line intensity of the second and fifth lines in the TMS spectra of the samples annealed at $T_a > 520\,^{\circ}$C (figure 8) is a sign of the moments' rotation out of the ribbon plane in the bulk. The second distinction is as regards the magnetic microstructure, and it is discussed in more detail below.

The average values of the hyperfine-field distributions $\langle B\rangle_f$ and the relative spectral areas A_f in figures 10(*a*) and (*b*), respectively, were derived from TMS (solid symbols, solid curves) and CEMS (open symbols, dashed curves) of X = Cu and Au alloys, and they are plotted against annealing temperature T_a for all individual spectral components f = AM, IF, and CR. The experimental errors of ± 0.1 T and $\pm 3\%$ are smaller than the symbols. The total value of the magnetic hyperfine field $B_{tot} = \Sigma_f\{A_f\langle B\rangle_f\}$ is also given.

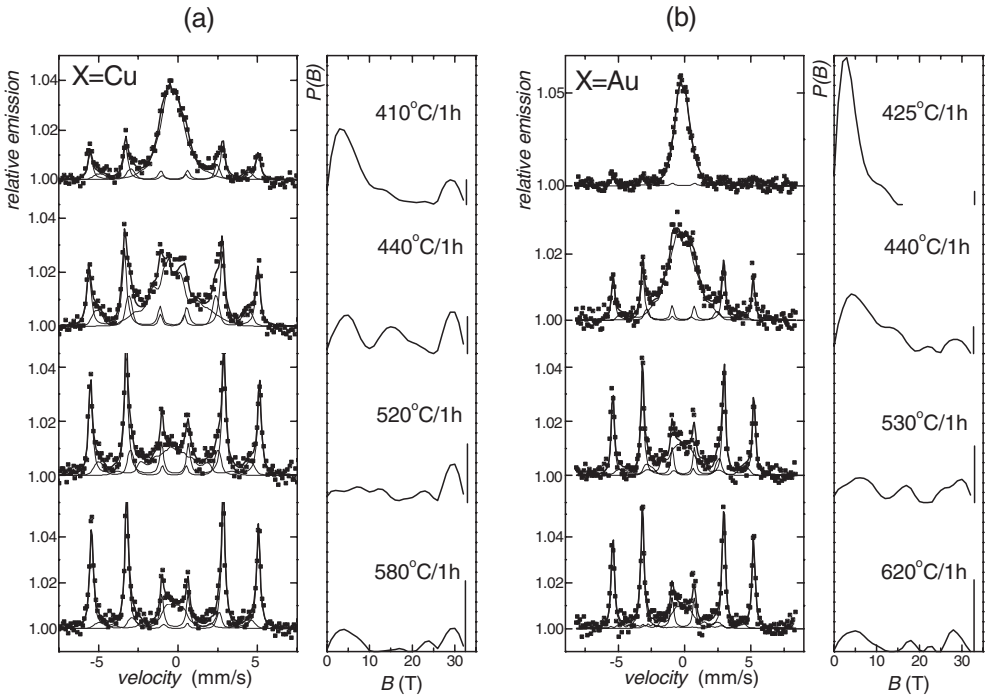

Figure 9. Room temperature CEMS (left side of panel) and corresponding distributions of hyperfine fields, $P(B)$ (right), for $Fe_{80}Mo_7X_1B_{12}$ alloy, with X = Cu (*a*), X = Au (*b*), annealed at the temperatures indicated for 1 h.

The hyperfine fields of the CR and IF components remain practically unchanged over the whole T_a-range for both the bulks (TMS) and the surfaces (CEMS) of the alloys studied. It should be noted that $\langle B\rangle_{IF}$ is smaller than B_{CR} by about 3.5 T. We assume that Fe atoms that establish the IF are situated on the surface of crystalline grains as well as in their immediate vicinity. That is why their magnetic hyperfine fields, though distorted due to non-unique structural positions, follow hyperfine fields of the CR phase despite the divergent development of A_{CR} and A_{IF} with the annealing temperature in figure 10(*b*). (Note that increase in A_{CR} does not necessarily imply increase in A_{IF}—because of, for example, clustering of the nanograins.) Hupe *et al* [20] found a close similarity between the CR and IF components in $Fe_{86-x}Cu_1Nb_xB_{13}$ nanocrystalline spectra, employing a new analysis strategy [21]. In the latter, spectral models are not described in advance as in [9] but are derived directly from the fitted spectra.

The temperature dependences of $\langle B\rangle_f$ and A_f are nearly identical (within the experimental error) for both alloys beyond $T_a \approx 500\,^{\circ}$C. As seen from figure 2, the first crystallization is almost completed at this temperature. The differences between $\langle B\rangle_{AM}$ and $\langle B\rangle_{tot}$ for X = Cu and Au observed at $T_a < 500\,^{\circ}$C stem primarily from the different quantity of CR in them. Thus, we can conclude that in the well-developed crystallization stage the influence of Cu and Au on the resulting hyperfine magnetic parameters as well as on A_{CR} cannot be discerned. The role of the element is crucial only in the first steps of the crystallization process. From this point of view, even though the magnetic microstructures of the two materials are very alike, the Cu-containing alloy seems to be more favourable because, as we discussed in the previous section, it provides as-quenched amorphous structure with fewer stress centres than the one containing Au.

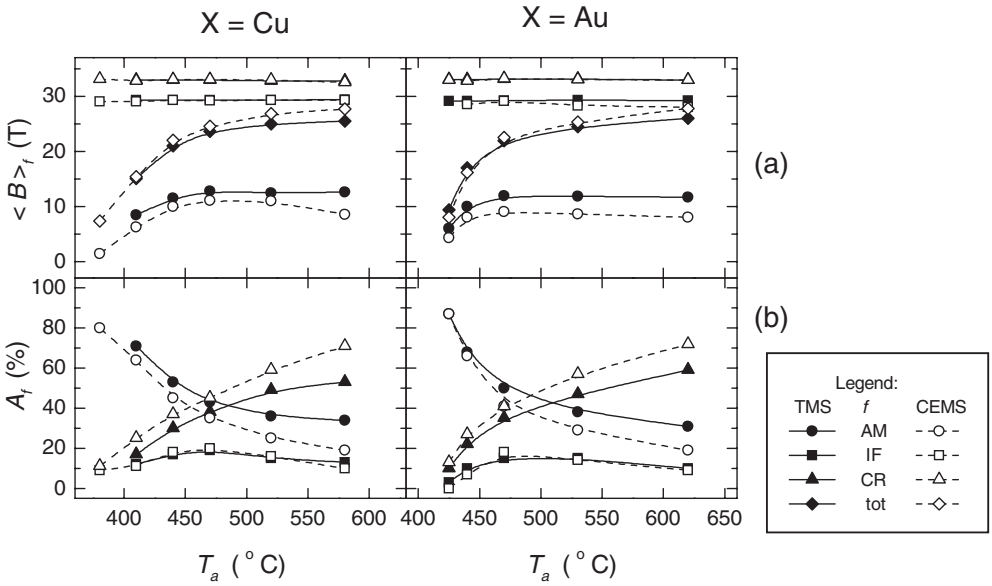

Figure 10. Average values, $\langle B\rangle_f$, of the hyperfine-field distributions $P(B)$ (*a*) and relative fractions of the spectral components A_f (*b*) plotted against annealing temperature, T_a, for $Fe_{80}Mo_7X_1B_{12}$ alloy, with X = Cu—left-hand panel—and X = Au—right-hand panel. For the meaning of the symbols f, see the text and the key. Solid symbols and curves: TMS; open symbols and dashed curves: CEMS.

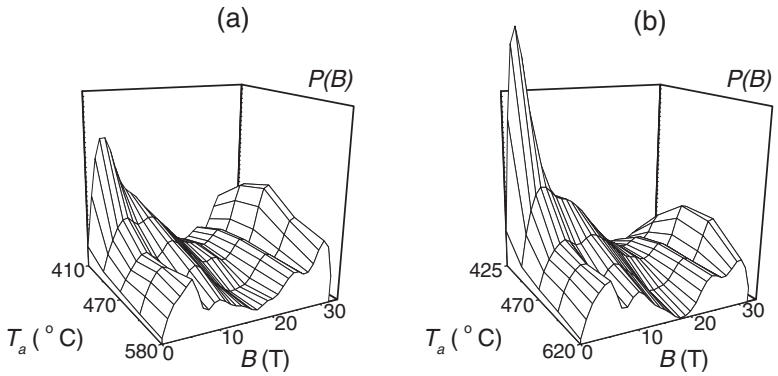

Figure 11. 3D mappings of hyperfine-field distributions $P(B)$ obtained from transmission Mössbauer spectra of $Fe_{80}Mo_7X_1B_{12}$ alloys; X = Cu (*a*), X = Au (*b*).

Finally, we shall compare the magnetic microstructures of the AM in $Fe_{80}Mo_7X_1B_{12}$, X = Cu, Au, nanocrystalline alloys with the help of $P(B)$ distributions. For that purpose, we use the three-dimensional (3D) mappings of the hyperfine-field distributions in figures 11 and 12 as derived from TMS and CEMS, respectively. They exhibit close similarity as regards qualitative features. Quantitative differences, which are most pronounced in the $P(B)$ intensity at the initial annealing temperature T_a, are caused by different CR contents in the X = Cu and Au alloys, especially in the early stage of crystallization.

Two sets of humps can be distinguished in the 3D $P(B)$ mappings obtained from the TMS (figure 11), namely low-field humps located at about 5 and 10 T, and high-

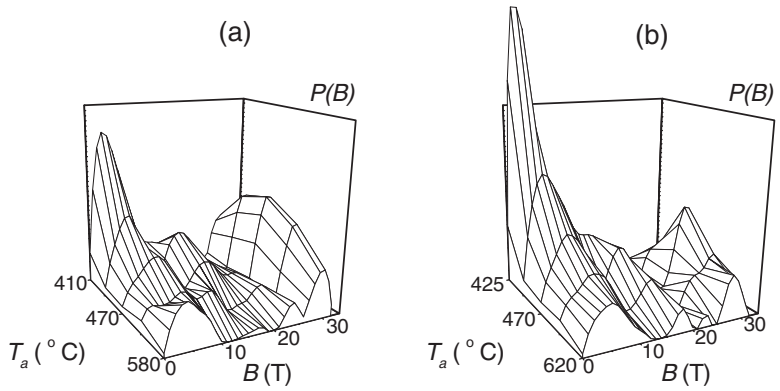

Figure 12. 3D mappings of hyperfine-field distributions $P(B)$ obtained from CEMS of $Fe_{80}Mo_7X_1B_{12}$ alloys; X = Cu (*a*), X = Au (*b*).

field humps positioned at about 25–30 T. This indicates that the AM and IF phases are chemically inhomogeneous.

The low-field components (especially that at about 5 T) can be assigned to Fe atoms that primarily have Mo as nearest neighbours. For low T_a, the residual AM resembles that of an as-quenched state and that is why the hump at low T_a is actually a representation of a $P(\Delta)$ distribution. As the amount of CR rises with increasing T_a, ferromagnetic exchange interactions influence the topology of the magnetic structure [16, 18] and regions with higher B-values appear in the AM. Moreover, as Fe atoms segregate into bcc CR grains, they leave regions depleted in Fe but enriched in other constituent elements behind. As a result, the chemical and/or topological SRO is modified. Atom-probe field-ion microscopy studies provide direct experimental evidence supporting this interpretation [22].

Fe atoms surrounded preferentially by other Fe or B atoms cover higher fields of about 25–30 T. The similar behaviour of the $P(B)$ distributions is discussed in more detail elsewhere [23] for $Fe_{80}Nb_7Cu_1B_{12}$ nanocrystalline alloy. Low-temperature measurements performed on the X = Cu alloy [24] favour this interpretation as well.

Closed domains [19] that tend to align magnetic moments into the plane of ribbon-shaped samples govern the surface magnetic structure. As a result, the distributions of the hyperfine fields are also affected, as seen from figure 12 where 3D mappings of the $P(B)$ distributions derived from CEMS spectra are given. Low (about 5 T) and high (about 30 T) humps are separated by regions of intermediate B-values that are not very well resolved. Thus, differences in SRO between bulk and surface are demonstrated also in magnetic microstructure.

4. Conclusions

We have studied the influence of whether X = Cu or Au on the structural and magnetic behaviour of amorphous and nanocrystalline $Fe_{80}Mo_7X_1B_{12}$ alloys. The initial temperature of crystallization determined by DSC is 410 and 430 °C for Cu and Au samples, respectively. CEMS experiments proved that surface crystallization appears about 25 °C earlier. The isothermal DSC trace confirmed that the crystallization kinetics was the same as for classical FINEMET-type alloys.

Room temperature ^{57}Fe Mössbauer spectrometry carried out in transmission geometry and using conversion electrons revealed microstructural differences for amorphous samples

annealed below the crystallization onset. Au-containing alloy shows a higher degree of structural inhomogeneity in the bulk as-quenched state than was observed for X = Cu. The inhomogeneity continually reduces during relaxation at temperatures up to 380 °C. The surface regions are structurally similar for the two alloys.

Annealing in the range of the first crystallization peaks has revealed the appearance of magnetic interactions even via the paramagnetic amorphous phase. They are due to magnetic exchange among bcc Fe nanograins created during annealing. Identification of the nanocrystals was performed by means of x-ray diffraction and Mössbauer spectrometry. The latter provided hyperfine magnetic fields also for disordered structural Fe positions. $P(B)$ distributions show qualitative similarities for X = Cu and Au. Quantitative differences arise on account of the different crystalline contents especially in the early stage of crystallization. Using 3D mappings of $P(B)$ distributions derived from TMS and CEMS, differences between bulk and surface magnetic behaviours were demonstrated.

Both alloys are excellent candidates for subjects of model studies, allowing detailed Mössbauer effect investigations of two-phase magnetic systems.

Acknowledgments

This work was supported by the grants Franc/Slov/1 and SGA No 1/8305/01.

References

[1] Suzuki K, Makino A, Inoue A and Masumoto T 1993 *J. Appl. Phys.* **74** 3316
[2] McHenry M E and Laughlin D E 2000 *Acta Mater.* **48** 223
[3] Suzuki K, Makino A, Inoue A and Masumoto T 1991 *J. Appl. Phys.* **70** 6232
[4] Suzuki K 1999 *Mater. Sci. Forum* **312–4** 521
[5] Würschum R 1995 *Nanostruct. Mater.* **6** 93
[6] Grenèche J-M, Miglierini M and Ślawska-Waniewska A 2000 *Hyperfine Interact.* **126** 27
[7] Suzuki K, Kataoka N, Inoue A, Makino A and Masumoto T 1990 *Mater. Trans. JIM* **31** 743
[8] Seberíni M and Degmová J 1997 *Czech. J. Phys.* **47** 559
[9] Miglierini M and Grenèche J-M 1997 *J. Phys.: Condens. Matter* **9** 2303
[10] Suzuki K and Cadogan J M 2000 *J. Appl. Phys.* **87** 7097
[11] Idzikowski B, Baszyński J, Škorvánek I, Müller K-M and Eckert D 1998 *J. Magn. Magn. Mater.* **177–81** 941
[12] Illeková E, Czomorová K, Kuhnast F A and Fiorani J M 1996 *Mater. Sci. Eng.* A **205** 166
[13] Illeková E, Cunat Ch, Kuhnast F A, Aharoune A and Fiorani J M 1992 *Thermochim. Acta* **203** 445
[14] Kopcewicz M and Grabias A 1996 *J. Appl. Phys.* **80** 3422
[15] Grabias A, Kopcewicz M and Idzikowski B 1999 *Nanostruct. Mater.* **12** 899
[16] Hernando A and Kulik T 1994 *Phys. Rev.* B **49** 7064
[17] Navarro I, Ortuño M and Hernando A 1996 *Phys. Rev.* B **53** 11 656
[18] Hernando A 1999 *J. Phys.: Condens. Matter* **11** 9455
[19] Gonser U and Schaaf P 1991 *Fresenius J. Anal. Chem.* **341** 131
[20] Hupe O, Chuev M A, Bremers H, Hesse J and Afanas'ev A M 1999 *J. Phys.: Condens. Matter* **11** 10 545
[21] Chuev M, Hupe O, Bremers H, Hesse J and Afanas'ev A M 2000 *Hyperfine Interact.* **126** 407
[22] Hono K, Zhang Y, Inoue A and Sakurai T 1995 *Mater. Trans. JIM* **36** 909
[23] Miglierini M and Grenèche J-M 1999 *Hyperfine Interact.* **122** 121
[24] Miglierini M, Seberíni M, Tóth I, Gröne R, Vitázek K, Grenèche J-M and Idzikowski B 2001 *Scr. Mater.* **44** 1353